Mathematical model of conductive fabric-based flexible pressure sensor

Michel Chipot[a], Kyounghun Lee[b,*], Jin Keun Seo[b]

[a] *Institut für Mathematik, Universität Zürich, Winterthurerstrasse 190*
[b] *Department of Computational Science and Engineering, Yonsei University, 50 Yonsei-Ro*

Abstract

This paper proposes a mathematical model of a pressure-sensitive conductive fabric sensor, which adopts the technique of electrical impedance tomography (EIT) with a composite fabric being capable of changing its effective electrical property due to an applied pressure. We model the composite fabric from an electrically conductive yarn and a sponge-like non-conductive fabric with high pore density, and the conductive yarn is woven in a wavy pattern to possess a pressure-sensitive conductive property, in the sense of homogenization theory. We use a simplified version of EIT technique to image the pressure distribution associated with the conductivity perturbation. A mathematical ground for the effective conductivity in one-direction is provided. We conduct an experiment to test the feasibility of the proposed pressure sensor.

Keywords: flexible sensor, pressure sensor, homogenized conductivity, asymptotic analysis, mathematical modeling

1. Introduction

There has been considerable attention drown to conductive fabric pressure sensors in the field of wearable sensors [16]. This type of sensors has several advantages including flexibility, low-cost, and washability. These devices

*Corresponding author
Email addresses: m.m.chipot@math.uzh.ch (Michel Chipot), imlkh@yonsei.ac.kr (Kyounghun Lee), seoj@yonsei.ac.kr (Jin Keun Seo)

have a wide range of applications, including in smart textiles[13, 8, 12], tactile sensors[3], artificial skins[18], and patient's movement monitoring technologies[14, 2]. It is intended to sense a pressure distribution exerted over the fabric surface by generating changes in electrical property over the touched area. This property is called piezoresistance [5] or piezoimpedance [19], depending on the frequency of the signal used to measure the electrical property variation, and in opposition to piezoelectricity, whose application in the field of wearables and e-textiles is extremely difficult due to materials science issues [6].

Recently, electrical impedance tomography (EIT) has been used to develop sensors monitoring pressure distribution[18, 20, 21]. While this type of sensors is fast and simple (requiring only a conductive fabric and a EIT system), it has difficulties in image reconstruction[11]. In this paper, we propose a mathematical model of a effective pressure mapping system that exploit EIT technique, but uses a simple reconstruction method for recovery of pressure distribution. This pressure mapping system is designed by a pressure-sensitive conductive fabric, taking into account changes in the effective conductivity due to the pressure exerted over the fabric surface. As shown in Figure 1 and 2, an electrically conductive yarn is woven into a sponge-like non-conductive fabric with high pore density so that its periodic wavy pattern is designed to produce a pressure sensitivity. The pressure sensing matrix is made by a double layer of these conductive fabrics patterned in rows and columns of the matrix. When a pressure due to contact is applied over the surface of the fabric, the effective admittivity changes over the corresponding squeezed area. We attach several electrodes to the boundary of the fabric, and adopt the technique of electrical impedance tomography[4, 11] to visualize the pressure distribution by measuring the pressure-induced admittivity changes.

For systematic studies for development of higher performance fabric sensors, we describe its mathematical framework by introducing a concept of directional effective conductivity. This theoretical study is intended to achieve higher performance sensors. We carry out theoretical study on directional homogenized admittivity property associated with the composite fabric with its periodic wave

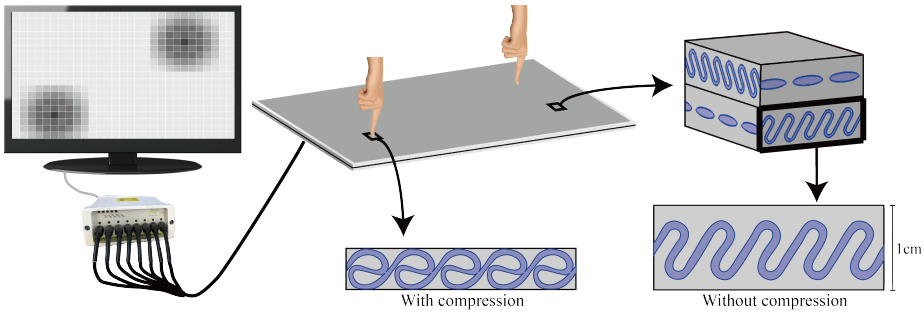

Figure 1: A schematic of the proposed pressure sensor

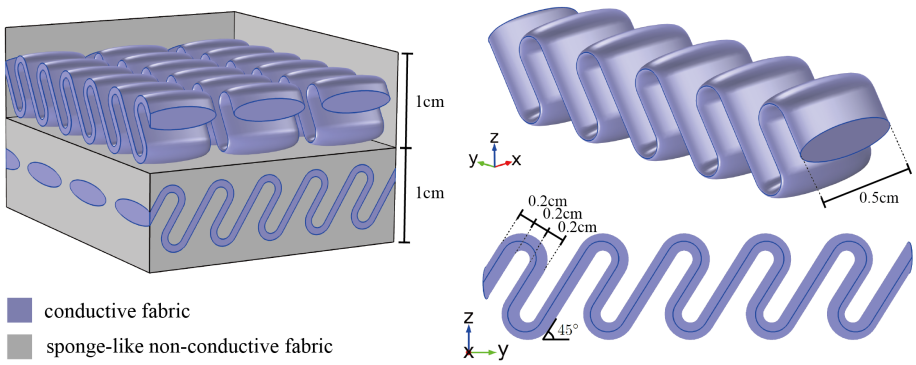

Figure 2: Structure of the composite fabric and the wave pattern of the conductive fabric

pattern.

2. Method

For a systematic study, let us describe the corresponding mathematical framework. For ease of explanation, we assume that the surface of the fabric sensor occupies the region $\Omega := \{(x, y) \ : -a < x < a, \ -b < y < b\}$ as shown in Figure 1. We inject two linearly independent currents of I mA at low-frequency in the x-direction and y-direction. Let σ_p denote the effective conductivity(see Remark 1) in response to the pressure distribution p. The effective conductivity is explained rigorously in Section 3. The proposed fabric sensor is designed

such that the resulting electrical potentials $v_p^{(1)}$ and $v_p^{(2)}$ approximately satisfy, respectively, the following equations:

$$\begin{cases} \frac{\partial}{\partial x}\left(\sigma_p(x,y)\frac{\partial}{\partial x}v_p^{(1)}(x,y)\right) = 0 & \text{for} \quad (x,y) \in \Omega, \\ \sigma_p(-a,y)\frac{\partial v_p^{(1)}}{\partial x}(-a,y) = I = \sigma_p(a,y)\frac{\partial v_p^{(1)}}{\partial x}(a,y) & \text{for} \quad -b < y < b, \end{cases} \tag{1}$$

$$\begin{cases} \frac{\partial}{\partial y}\left(\sigma_p(x,y)\frac{\partial}{\partial y}v_p^{(2)}(x,y)\right) = 0 & \text{for} \quad (x,y) \in \Omega, \\ \sigma_p(x,-b)\frac{\partial v_p^{(2)}}{\partial y}(x,-b) = I = \sigma_p(x,b)\frac{\partial v_p^{(2)}}{\partial y}(x,b) & \text{for} \quad -a < x < a. \end{cases} \tag{2}$$

The equation (1) expresses that the induced electrical current flows only in the x-direction, whereas the equation (2) describes the induced electrical current flows in the y-direction. Note that the equation (1) has a unique solution up to functions of the y-variable (i.e., if $v_p^{(1)}(x,y)$ and $\widetilde{v}_p^{(1)}(x,y)$ are solutions to (1), then $v_p^{(1)}(x,y) - \widetilde{v}_p^{(1)}(x,y) = f(y)$ for a function $f(y)$). Similarly, (2) has a unique solution up to functions of the x variable.

Remark 1. *From the structure of the composite fabric shown in Figure 2, electrical currents flow along the wavy conductive fabrics. Hence, currents flows only in the x-direction on the top layer, whereas currents flow only in the y-direction on the bottom layer. Assume that we inject a current of I mA in the*

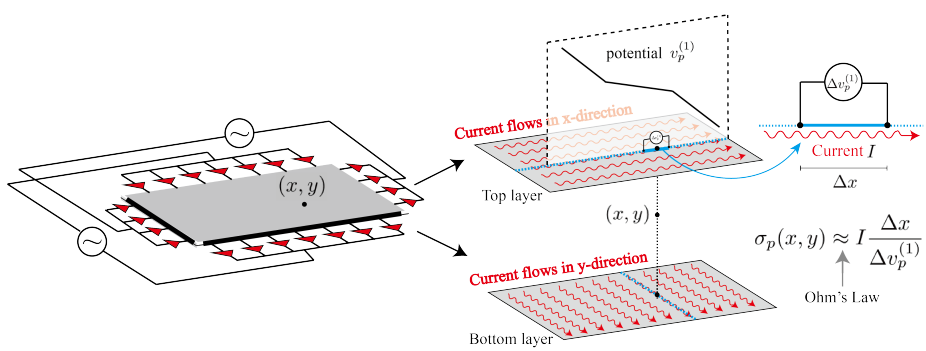

Figure 3: The two currents flowing independently on the top layer (in the x-direction) and on the bottom layer (in the y-direction) of the fabric sensor, and the effective conductivity σ_p at (x,y)

x-direction to the top layer of the sensor as shown in Figure 3. Let $v_p^{(1)}$ denote the resulting potential due to this current. According to Ohm's law, the effective conductivity σ_p at (x, y) can be expressed approximately as:

$$\sigma_p(x, y) \approx I \frac{\Delta x}{\Delta v_p^{(1)}(x, y)}, \tag{3}$$

where $\Delta v_p^{(1)}(x, y) = v_p^{(1)}(x - \frac{\Delta x}{2}, y) - v_p^{(1)}(x + \frac{\Delta x}{2}, y)$. This relation (3) leads to

$$\sigma_p(x, y) \frac{\Delta v_p^{(1)}(x, y)}{\Delta x} \approx I\,(constant) \tag{4}$$

Therefore, $v_p^{(1)}$ approximately satisfies $\frac{\partial}{\partial x}(\sigma_p(x, y) \frac{\partial v_p^{(1)}}{\partial x}(x, y)) = 0$. Similarly, the potential $v_p^{(2)}$ on the bottom layer approximately satisfies $\frac{\partial}{\partial y}(\sigma_p(x, y) \frac{\partial v_p^{(2)}}{\partial y}(x, y)) = 0$ with the same conductivity σ_p (i.e. the top and bottom layers are assumed to have the same pressure response).

In the proposed fabric sensor, we measure the following potential differences on the boundary:

$$V_p^{(1)}(y) = v_p^{(1)}(a, y) - v_p^{(1)}(-a, y) \quad \text{and} \quad V_p^{(2)}(x) = v_p^{(2)}(x, b) - v_p^{(2)}(x, -b). \tag{5}$$

Similarly, the potential differences $V_0^{(1)}$ and $V_0^{(2)}$ in the absence of pressure $(p = 0)$ are, respectively, denoted by

$$V_0^{(1)}(y) = v_0^{(1)}(a, y) - v_p^{(1)}(-a, y) \quad \text{and} \quad V_0^{(2)}(x) = v_0^{(2)}(x, b) - v_0^{(2)}(x, -b), \tag{6}$$

where $v_0^{(1)}$ and $v_0^{(2)}$ are the corresponding potentials of (1) and (2). When a pressure is exerted over the fabric surface, the fabric is compressed. In this compressed region, the air goes out and the conductive yarns touch each other, making the current paths shorter or generating other current paths. This results in conductivity increase at the compressed region and the decrease of the measured voltage, namely, at (x, y), a position in the compressed region,

$$V_p^{(1)}(y) - V_0^{(1)}(y) < 0 \quad \text{and} \quad V_p^{(2)}(x) - V_0^{(2)}(x) < 0. \tag{7}$$

To be more specific, for each y, the sign of the voltage difference $\delta V_p^{(1)}(y) := V_p^{(1)}(y) - V_0^{(1)}(y)$ associated with the x-directional current determines whether

a pressure is applied in the line segment $L_y := \{(x, y) \ : \ -a < x < a\}$ shown in Figure 4. In the same way, for each x, the voltage difference $\delta V_p^{(2)}(x) := V_p^{(2)}(x) - V_0^{(2)}(x)$ associated with y-directional current determines whether a pressure is applied in the line segment $L_x := \{(x, y) \ : \ -b < y < b\}$. Both signs of $\delta V_p^{(1)}(y)$ and $\delta V_p^{(2)}(x)$ become negative when a pressure is applied over a region which contains (x, y), the intersection of the line segments L_y and L_x.

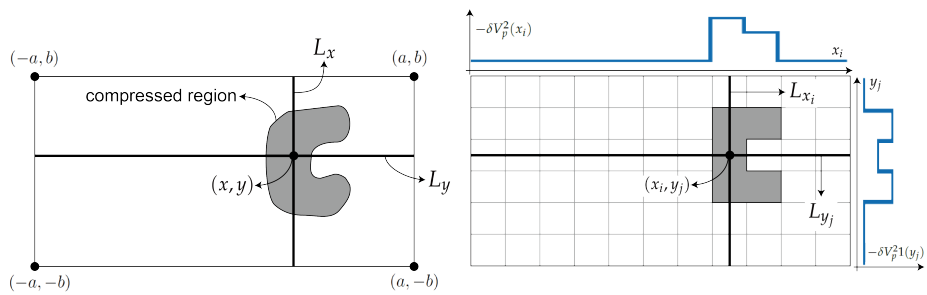

Figure 4: The domain Ω and the line segments L_x, L_y with their intersection point (x, y), where the colored region depicts the compressed region. The right figure is the domain after discretization.

For ease of explanation, we consider the simplest discrete setting, where the pressure image $p = (p_{ij})_{1 \le i \le N_x, 1 \le j \le N_y}$ are discrete with $p_{ij} \in \{0, 1\}$. The discrete pressure p_{ij} can be viewed as $p_{ij} = p(x_i, y_j)$ with $x_i = -a + (2i-1)a/N_x$ and $y_j = -b + (2j-1)b/N_y$. Here, $p_{ij} \in \{0, 1\}$ means that the fabric can have only the two states: not compressed or totally compressed. In this situation, the voltage differences $\delta V_p^{(1)}(y_j)$ and $\delta V_p^{(2)}(x_i)$ can be considered as a multiple of the numbers of pressured positions along the line segments L_{y_j} and L_{x_i}, respectively:

$$\delta V_p^{(1)}(y_j) = (-\beta) \left| \{i \ : \ p_{ij} = 1\} \right|, \tag{8}$$

$$\delta V_p^{(2)}(x_i) = (-\beta) \left| \{j \ : \ p_{ij} = 1\} \right|, \tag{9}$$

where $|A|$ denotes the cardinality of the set A, β is a positive constant and represents the amount voltage change for the pressure applied at one pixel.

In Figure 4, we have drawn graphs of $-\delta V_p^{(1)}(y_j)$ and $-\delta V_p^{(2)}(x_i)$, which show the relations (8) and (9). The proposed fabric sensor is designed to have the following important properties:

(i) If $p_{ij} = 1$, then $\delta V_p^{(1)}(y_j)\delta V_p^{(2)}(x_i) \neq 0$.

(ii) If $\delta V_p^{(1)}(y_j) = 0$, then $p_{ij} = 0$ along L_{y_j}.

(iii) If $\delta V_p^{(2)}(x_i) = 0$, then $p_{ij} = 0$ along L_{x_i}.

The property (i) comes from (7). The property (ii) means that if the voltage difference $\delta V_p^{(1)}(y_j)$ is zero, no pressure is applied over the line L_{y_j}. Similarly, the property (iii) means that no pressure is applied over L_{x_i} when the voltage difference is zero, $\delta V_p^{(2)}(x_i) = 0$.

Now, we are ready to explain our reconstruction method. We adapts the idea of back-projection [22] used in the computerized tomography. The proposed reconstruction method is based on the following adapted back-projection formula, which takes into account the above properties (i), (ii), (iii) and the relations (8), (9):

$$\widetilde{p}_{ij} := \begin{cases} \frac{1}{2\beta}\left(\frac{-\delta V_p^{(1)}(y_j)}{\left|\left\{k \,:\, \delta V_p^{(2)}(x_k)\neq 0\right\}\right|} + \frac{-\delta V_p^{(2)}(x_i)}{\left|\left\{k \,:\, \delta V_p^{(1)}(y_k)\neq 0\right\}\right|}\right) & \text{if} \quad \delta V_p^{(1)}(y_j)\ \delta V_p^{(2)}(x_i) \neq 0 \\ 0 & \text{otherwise.} \end{cases} \tag{10}$$

The relation between $\widetilde{p}_{ij}$ and p_{ij} can be shown by substituting (8) and (9) for $\delta V_p^{(1)}(y_j)$ and $\delta V_p^{(2)}(x_i)$, respectively, in (10). In this process, β is canceled out in the output value $\widetilde{p}_{ij}$.

$$\begin{aligned} \widetilde{p}_{ij} =& \frac{1}{2\beta}\left(\frac{-\delta V_p^{(1)}(y_j)}{\left|\left\{k \,:\, \delta V_p^{(2)}(x_k) \neq 0\right\}\right|} + \frac{-\delta V_p^{(2)}(x_i)}{\left|\left\{k \,:\, \delta V_p^{(1)}(y_k) \neq 0\right\}\right|}\right) \\ =& \frac{1}{2}\left(\frac{|\{k \,:\, p_{kj} = 1\}|}{|\{k \,:\, (\beta\,|\{\ell \,:\, p_{k\ell} = 1\}||) \neq 0\}} + \frac{|\{k \,:\, p_{ik} = 1\}|}{|\{k \,:\, (\beta\,|\{\ell \,:\, p_{\ell k} = 1\}|) \neq 0\}|}\right) \\ =& \frac{1}{2}\left(\frac{|\{k \,:\, p_{kj} = 1\}|}{|\{k \,:\, |\{\ell \,:\, p_{k\ell} = 1\}| \neq 0\}|} + \frac{|\{k \,:\, p_{ik} = 1\}|}{|\{k \,:\, |\{\ell \,:\, p_{\ell k} = 1\}| \neq 0\}|}\right) \end{aligned} \tag{11}$$

It follows from the fact that $|\{\ell \,:\, p_{k\ell} = 1\}| \neq 0$ is equivalent to that $p_{k\ell} = 1$ for some ℓ.

$$\widetilde{p}_{ij} = \frac{1}{2}\left(\frac{|\{k \,:\, p_{kj} = 1\}|}{|\{k \,:\, p_{k\ell} = 1 \text{ for some } \ell\}|} + \frac{|\{k \,:\, p_{ik} = 1\}|}{|\{k \,:\, p_{\ell k} = 1 \text{ for some } \ell\}|}\right) \tag{12}$$

In the case that the pressure is applied at only one pixel, the proposed algorithm exactly recovers the pressure distribution, $\widetilde{p}_{ij} = p_{ij}$.

Figure 5 shows the above back projection method(10). For each j, we back-project the data $\delta V_p^{(1)}(y_j)$ to the all pixels $\left\{p_{ij} : \delta V_p^{(2)}(x_i) \neq 0\right\}$ along the horizontal direction. Next, for each i, we backproject the data $\delta V_p^{(2)}(x_i)$ to the all pixels $\left\{p_{ij} : \delta V_p^{(1)}(y_j) \neq 0\right\}$ along the vertical direction. The value of $\widetilde{p}_{ij}$ can be viewed as a scaled version of the sum of these two backprojections.

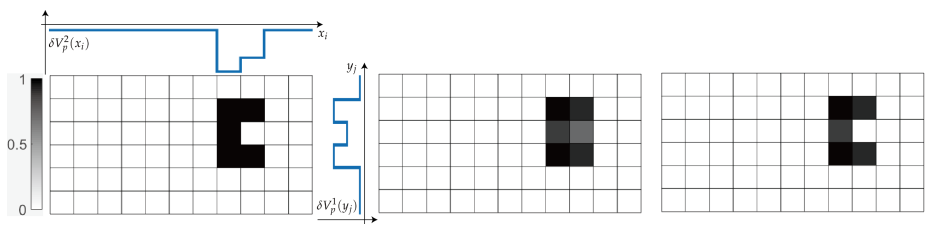

(a) p_{ij} (b) $\widetilde{p}_{ij}$ (c)

Figure 5: Adapted back-projection method. (a) The true pressure distribution in discretization; (b) Image correction using the data.

As shown in Figure 5(b), the reconstructed image of $\widetilde{p}_{i,j}$ is somewhat different from the true p_{ij}. One may reduce the mismatch using the knowledge of $|\{i : p_{ij} = 1\}|$ for all j and $|\{j : p_{ij} = 1\}|$ for all i. Figure 5(c) shows a corrected image. However, in general, the two directional data are insufficient to recover p_{ij} correctly. To identify p_{ij} accurately, we may use a few more layers in the fabric sensor to produce the current-voltage data in more directions. Then the adapted back-projection method can recover the pressure distribution accurately.

Remark 2. *The conductivity of conductive layer, the wave pattern of the conductive fabric, and the thickness of the layers affect the effective conductivity and the measured voltages. More importantly, the wave pattern of the conductive fabric dominantly determines the amount of change in the effective conductivity and the measured voltage due to compression in the way that how much the conductive fabrics are touching each other after compression. To be more specific,*

we have drawn figures of 2D cross sections of the composite fabrics without and with compression, as shown in Figure 6. When a current flows in transverse direction, it flows along the conductive fabric depicted as arrowed lines colored in red in Figure 6. After compression, the conductive fabrics touch each other generating other current paths as shown in the right figure in Figure 6. This results in an increase of the effective conductivity after compression.

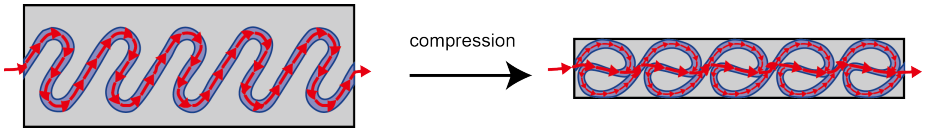

Figure 6: Cross sections of the composite fabrics without and with compression

In particular, the wave pattern affects the amount of voltage change for the pressure applied at one pixel, which we denoted by β. In the proposed model, if β is bigger than measurement errors or noises, β does not significantly affect the final output value $\widetilde{p}_{ij}$ obtained by the reconstruction algorithm (10) since the algorithm includes the division process by β.

3. Directional effective conductivity

In this section, we explain the directional effective conductivity σ_p introduced in (1) and (2) in the previous section. Let us consider a point $(x, y) \in \Omega$ over the fabric surface. Taking a closer look inside of it, the point (x, y) can be considered as a voxel of double layers of composite fabrics in micro-scale, shown in Figure 7. Since currents flow independently through each fabric sheet layer and each layer consists of conductive yarns with a periodic pattern, let us focus on a single conductive yarn for ease of analysis. As shown in Figure 7, a rectangular domain in two-dimension represents the vertical cross-section of a piece of the composite fabric sheet consisting of a sponge-like non-conductive fabric with air gaps(gray) and a conductive yarn(blue).

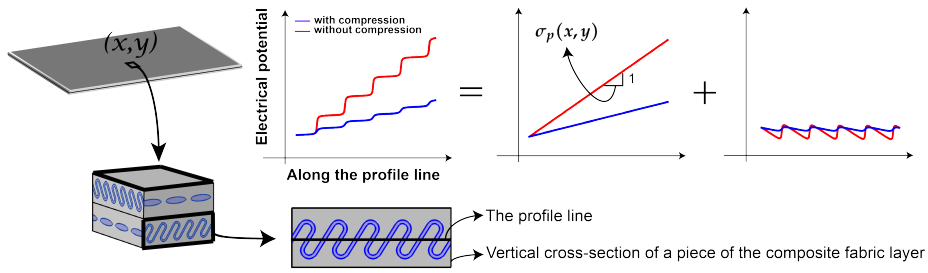

Figure 7: Vertical cross-section of a piece of the composite fabric sheet and the potential profile.

Consider that a transverse current flows from the right to the left side of the rectangular domain. The behavior of the current can be seen by drawing a graph of the corresponding potential. We show in Figure 7 the potentials over a profile line with and without compression. In either case, the potential over the profile line is oscillatory due to the periodic pattern of high and low conductive regions. In macroscale, these oscillations are insignificant and the potentials are considered as linear. By using Ohm's law, we define the directional effective conductivity as the inverse of the slope of the linear function. We perform this process rigorously using an asymptotic analysis in the following subsection. In Figure 7, with compression, the inverse of the slope is bigger than without-compression, which implies increase of the effective conductivity after compression.

Local changes in the effective conductivity come from structural changes in the conductive fabric subject to pressure. With an applied pressure, the wavy conductive fabrics are compressed and come into contact with each other. Hence, the local pressure results in the increase of the conductivity.

3.1. Asymptotic analysis

To explain the directional effective conductivity rigorously, we consider a simplified model. Let $\mathcal{Y}_\ell$ be the domain defined as $\mathcal{Y}_\ell = \{x \ : -\ell < x < \ell\} \times \Theta$ with $\Theta = \{z \ : 0 < z < 1\}$, $\Gamma_\ell^\pm = \{\pm\ell\} \times \Theta$ (see Figure 8). Let σ be the

point-wise conductivity in the region $\mathcal{Y}_\ell$, and assume that σ is periodic in the x direction such that

$$\sigma(x+1,z) = \sigma(x,z) \quad \text{for} \quad (x,z) \in \mathcal{Y}_\ell. \tag{13}$$

We also assume

$$0 < \lambda \leq \sigma \leq \Lambda \quad \text{for some positive constants} \;\; \lambda, \Lambda. \tag{14}$$

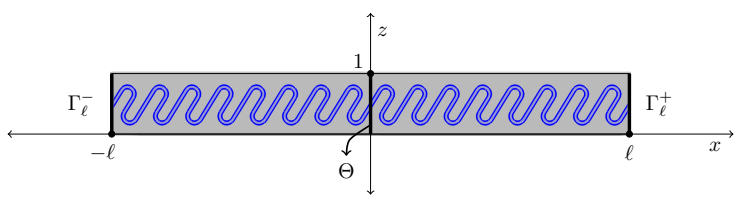

Figure 8: The domain $\mathcal{Y}_\ell$

We consider the potential u_ℓ satisfying the following Neumann boundary value problem:

$$\begin{cases} \nabla \cdot (\sigma \nabla u_\ell) &= 0 \quad \text{in} \quad \mathcal{Y}_\ell, \\ \mathbf{n} \cdot (\sigma \nabla u_\ell) &= \pm 1 \quad \text{on} \quad \Gamma_\ell^\pm, \\ \mathbf{n} \cdot (\sigma \nabla u_\ell) &= 0 \quad \text{on} \quad \partial \mathcal{Y}_\ell \setminus \left(\Gamma_\ell^+ \cup \Gamma_\ell^-\right), \end{cases} \tag{15}$$

where $\mathbf{n}$ is the outward unit normal to $\partial \mathcal{Y}_\ell$. The solution u_ℓ of (15) is unique within the following Hilbert space

$$\mathcal{S}_\ell = \left\{ \varphi \in H^1(\mathcal{Y}_\ell) \;:\; \int_\Theta \varphi(0,z)\, dz = 0 \right\}, \tag{16}$$

where H^1 denotes the standard Sobolev space of order 1 (See Ref. [1, 15]).

The domain $\mathcal{Y}_\ell$ can be considered as a piece of vertical cross-section of the fabric sensor after scaling, as shown in Figure 9. By scaling, we fix the thickness as 1 and consider the length as 2ℓ. When we regard the fabric sensor as a surface and its thickness h is almost zero ($h \to 0$), we can regard the length 2ℓ of $\mathcal{Y}_\ell$ as almost infinity ($\ell \to \infty$). In the scaled domain $\mathcal{Y}_\ell$, we analyze the behavior of the potential u_ℓ when ℓ goes to infinity, and define the directional effective conductivity.

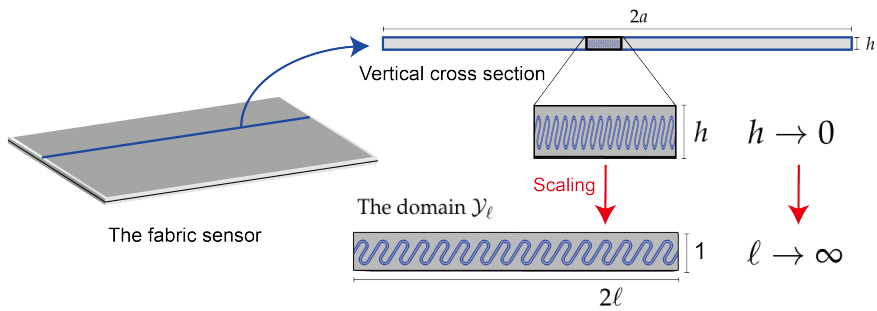

Figure 9: The domain $\mathcal{Y}_\ell$ and scaling.

We claim that

(i) u_ℓ converges as ℓ goes to infinity (in some sense).

(ii) ∇u_∞ is periodic in the x, where $u_\infty := \lim_{\ell\to\infty} u_\ell$.

(iii) u_∞ can be expressed as $u_\infty = u^p + u^h$, where u^p periodic in the x-direction and u^h is harmonic with respect to the x variable.

The claim (iii) tells that u_∞ can be viewed as a harmonic function u^h (with respect to the x variable) in macro-scale. The directional effective conductivity can be defined as the inverse of the slope of u^h. We restate the claims precisely, and verify them one by one.

Theorem 3. *u_ℓ converges in $H^1(\mathcal{Y}_{\ell_0})$ for any $\ell_0 \le \frac{\ell}{2}$.*

The convergence of u_ℓ can be verified by showing that ∇u_ℓ is a Cauchy sequence in L^2-norm, then the convergence of u_ℓ follows from the norm equivalence between the H^1-norm and the gradient norm $\|\nabla u\|_{L^2(\mathcal{Y}_\ell)}$ in the space $\mathcal{S}_\ell$.

Proof. Let u_ℓ be the weak solution in $\mathcal{S}_\ell$ to (15):

$$u_\ell \in \mathcal{S}_\ell, \quad \int_{\mathcal{Y}_\ell} \sigma \nabla u_\ell \cdot \nabla \varphi + \int_{\Gamma_\ell^-} \varphi - \int_{\Gamma_\ell^+} \varphi = 0 \quad \forall \varphi \in \mathcal{S}_\ell. \tag{17}$$

We first show that ∇u_ℓ is a Cauchy sequence in $L^2(\mathcal{Y}_{\ell_0})$ for any $\ell_0 \le \frac{\ell}{2}$. Let $0 \le \eta \le 1$. For $\ell_1 \le \ell - 1$, ρ_{ℓ_1} is the following function of x.

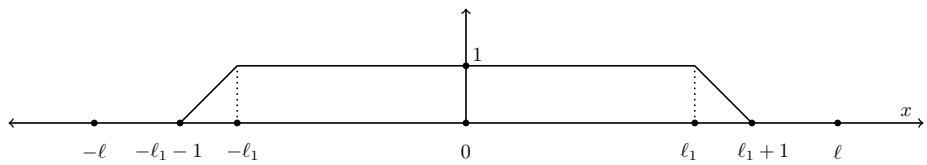

Figure 10: The test function ρ_{ℓ_1}

Then $(u_\ell - u_{\ell+\eta})\rho$ is a test function for the problem in $\mathcal{Y}_\ell$ and $\mathcal{Y}_{\ell+\eta}$. By subtraction we get

$$\int_{\mathcal{Y}_\ell} \sigma \nabla(u_\ell - u_{\ell+\eta}) \cdot \nabla\left((u_\ell - u_{\ell+\eta})\rho\right) = 0$$

$$\begin{aligned}
\Rightarrow \int_{\mathcal{Y}_{\ell_1+1}} \sigma |\nabla(u_\ell - u_{\ell+\eta})|^2 \rho &= -\int_{D_{\ell_1}} \sigma \partial_x (u_\ell - u_{\ell+\eta})(\partial_x \rho)(u_\ell - u_{\ell+\eta}) \\
&= -\int_{D^-_{\ell_1}} \sigma \partial_x (u_\ell - u_{\ell+\eta})(u_\ell - u_{\ell+\eta}) \\
&\qquad + \int_{D^+_{\ell_1}} \sigma \partial_x (u_\ell - u_{\ell+\eta})(u_\ell - u_{\ell+\eta})
\end{aligned}$$

where $D_{\ell_1} = \mathcal{Y}_{\ell_1+1} \setminus \mathcal{Y}_{\ell_1}$, $D^+_{\ell_1} = \{(x,y) \in D_{\ell_1} \ : \ x > 0\}$, and $D^-_{\ell_1} = \{(x,y) \in D_{\ell_1} \ : \ x < 0\}$.

Claim : $\displaystyle\int_{D^\pm_{\ell_1}} \sigma \partial_x (u_\ell - u_{\ell+\eta}) = 0.$

Take as test function of x in Figure 11 contained in the both $\mathcal{Y}_\ell$ and $\mathcal{Y}_{\ell+\eta}$ the functions below

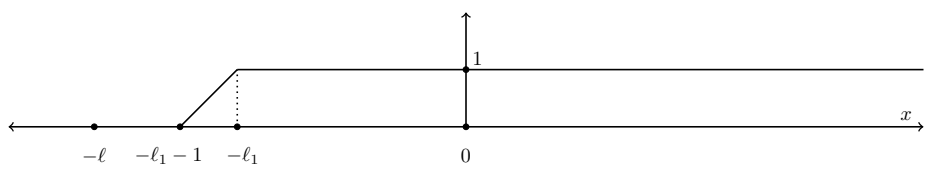

Figure 11: test function

we get

$$\int_{D^-_{\ell_1}} \sigma \partial_x u_\ell - \int_{\Gamma^+_\ell} 1 = 0, \quad \int_{D^-_{\ell_1}} \sigma \partial_x u_{\ell+\eta} - \int_{\Gamma^+_{\ell+\eta}} 1 = 0$$

By subtraction the claim follows for $D^-_{\ell_1}$. A similar proof goes for $D^+_{\ell_1}$.

Thus below (17) it follows that for any constants C_-, C_+ one has

$$\int_{\mathcal{Y}_{\ell_1+1}} \sigma|\nabla(u_\ell - u_{\ell+\eta})|^2\rho = \int_{D^-_{\ell_1}} \sigma\partial_x(u_\ell - u_{\ell+\eta})(u_\ell - u_{\ell+\eta} - C_-) \\ - \int_{D^+_{\ell_1}} \sigma\partial_x(u_\ell - u_{\ell+\eta})(u_\ell - u_{\ell+\eta} - C_+)$$

and thus by (14)

$$\lambda \int_{\mathcal{Y}_{\ell_1}} |\nabla(u_\ell - u_{\ell+\eta})|^2 \le \Lambda\|\partial_x(u_\ell - u_{\ell+\eta})\|_{L^2(D^-_{\ell_1})}\|(u_\ell - u_{\ell+\eta} - C_-)\|_{L^2(D^-_\ell)} \\ + \Lambda\|\partial_x(u_\ell - u_{\ell+\eta})\|_{L^2(D^+_{\ell_1})}\|(u_\ell - u_{\ell+\eta} - C_+\|_{L^2(D^+_\ell)},$$

where $\| \ \|_{L^2(A)}$ denotes the usual $L^2(A)$-norm (See Ref. [7, 9]).

Taking $C_\pm = \fint_{D^\pm_{\ell_1}} u_\ell - u_{\ell+\eta}$, $\left(\fint_A := \frac{1}{|A|}\int_A\right)$ we obtain easily by the Poincaré-Wirtinger inequality

$$\int_{\mathcal{Y}_{\ell_1}} |\nabla(u_\ell - u_{\ell+\eta})|^2 \le C\int_{D_{\ell_1}} |\nabla(u_\ell - u_{\ell+\eta})|^2,$$

with $C = C(\lambda, \Lambda)$. Writing $\int_{D_{\ell_1}} \cdot = \int_{\mathcal{Y}_{\ell_1+1}} \cdot - \int_{\mathcal{Y}_{\ell_1}} \cdot$, it comes with $\gamma = \frac{C}{1+C} < 1$

$$\int_{\mathcal{Y}_{\ell_1}} |\nabla(u_\ell - u_{\ell+\eta})|^2 \le \gamma\int_{\mathcal{Y}_{\ell_1+1}} |\nabla(u_\ell - u_{\ell+\eta})|^2.$$

Then starting from $\ell_1 = \frac{\ell}{2}$ and doing $\left[\frac{\ell}{2}\right]$ iterations ([ ] the integer part of a number) one gets

$$\int_{\mathcal{Y}_{\ell/2}} |\nabla(u_\ell - u_{\ell+\eta})|^2 \le \gamma^{\left[\frac{\ell}{2}\right]}\int_{\mathcal{Y}_{\frac{\ell}{2}+\left[\frac{\ell}{2}\right]}} |\nabla(u_\ell - u_{\ell+\eta})|^2.$$

Since $\frac{\ell}{2} - 1 < \left[\frac{\ell}{2}\right] \le \frac{\ell}{2}$ one obtains

$$\int_{\mathcal{Y}_{\ell/2}} |\nabla(u_\ell - u_{\ell+\eta})|^2 \le \frac{1}{\gamma}\gamma^{\frac{\ell}{2}}\int_{\mathcal{Y}_\ell} |\nabla(u_\ell - u_{\ell+\eta})|^2. \tag{18}$$

We estimate now u_ℓ. Taking $v = u_\ell$ in (15) we get

$$\lambda\int_{\mathcal{Y}_\ell} |\nabla u_\ell|^2 \le \int_{\mathcal{Y}_\ell} \sigma|\nabla u_\ell|^2 = \int_{\Gamma^+_\ell} u_\ell - \int_{\Gamma^-_\ell} u_\ell, \\ = \int_{\mathcal{Y}_\ell} \partial_x u_\ell \le |\mathcal{Y}_\ell|^{1/2}\left(\int_{\mathcal{Y}_\ell} |\nabla u_\ell|^2\right)^{1/2},$$

where $|\ |$ denotes the measure of sets (See Ref. [9]). Thus we get

$$\int_{\mathcal{Y}_\ell} |\nabla u_\ell|^2 \leq \frac{|\mathcal{Y}_\ell|}{\lambda^2} = \frac{2\ell}{\lambda^2}.$$

From (18) we deduce

$$\begin{aligned}
\int_{\mathcal{Y}_{\ell/2}} |\nabla(u_\ell - u_{\ell+\eta})|^2 &\leq \frac{1}{\gamma} e^{-\frac{\ell}{2}\ln\left(\frac{1}{\gamma}\right)}\ 2\int_{\mathcal{Y}_\ell} |\nabla u_\ell|^2 + |\nabla u_{\ell+\eta}|^2 \\
&\leq Ce^{-\frac{\ell}{2}\ln\frac{1}{\gamma}}\left\{\ell+\ell+\eta\right\} = Ce^{-\ell\alpha'}(2\ell+\eta) \ \text{ with } \ \alpha' = \frac{1}{2}\ln\frac{1}{\gamma} \\
&\leq Ce^{-\ell\alpha} \ \text{ for } \ \alpha < \alpha'.
\end{aligned}$$

We have obtained that

$$\|\nabla\left(u_\ell - u_{\ell+\eta}\right)\|_{L^2(\mathcal{Y}_{\ell/2})} \leq Ce^{-\ell\alpha} \ \text{ for } \ 0 \leq \eta \leq 1.$$

Thus for any t we obtain

$$\begin{aligned}
\|\nabla\left(u_\ell - u_{\ell+t}\right)\|_{L^2(\mathcal{Y}_{\ell/2})} &\leq \|\nabla\left(u_\ell - u_{\ell+1}\right)\|_{L^2(\mathcal{Y}_{\ell/2})} + \|\nabla\left(u_{\ell+1} - u_{\ell+2}\right)\|_{L^2(\mathcal{Y}_{\ell/2})} + \cdots \\
&\qquad + \left\|\nabla\left(u_{\ell+[t]} - u_{\ell+t}\right)\right\|_{L^2(\mathcal{Y}_{\ell/2})}, \\
&\leq \|\nabla\left(u_\ell - u_{\ell+1}\right)\|_{L^2(\mathcal{Y}_{\ell/2})} + \|\nabla\left(u_{\ell+1} - u_{\ell+2}\right)\|_{L^2(\mathcal{Y}_{(\ell+1)/2})} + \cdots \\
&\qquad + \left\|\nabla\left(u_{\ell+[t]} - u_{\ell+t}\right)\right\|_{L^2(\mathcal{Y}_{(\ell+[t])/2})}, \\
&\leq Ce^{-\alpha\ell} + Ce^{-\alpha(\ell+1)} + \cdots + Ce^{-\alpha(\ell+[t])}, \\
&\leq Ce^{-\alpha\ell}\ \frac{1}{1-e^{-\alpha}}, \\
&= \widetilde{C}e^{-\alpha\ell} \ \text{ for } \ \widetilde{C} = \frac{C}{1-e^{-\alpha}}.
\end{aligned}$$

Then, ∇u_ℓ is a Cauchy sequence in the $L^2(\mathcal{Y}_{\ell_0})$ for any $\ell_0 \leq \frac{\ell}{2}$. It only remains to show that the gradient norm $\|\nabla\cdot\ \|_{L^2(\mathcal{Y}_\ell)}$ is equivalent to the $H^1(\mathcal{Y}_\ell)$-norm in the space $\mathcal{S}_\ell$: for $\varphi \in \mathcal{S}_\ell$,

$$\|\nabla\varphi\|_{L^2(\mathcal{Y}_\ell)} \lesssim \|\varphi\|_{H^1(\mathcal{Y}_\ell)}, \tag{19}$$

$$\|\nabla\varphi\|_{L^2(\mathcal{Y}_\ell)} \gtrsim \|\varphi\|_{H^1(\mathcal{Y}_\ell)}, \tag{20}$$

where the expression $X \lesssim Y$ is used to mean that there is a positive constant C independent of φ such that $X \leq CY$. The inequality (19) is straightforward,

and (20) comes from the fact that $\int_\Theta \varphi(0,z)\,dz = 0$. To be more precisely, if we assume that (20) does not hold, for each positive integer n there exists $\varphi_n \in \mathcal{S}_\ell$ such that

$$\|\nabla\varphi_n\|_{L^2(\mathcal{Y}_\ell)} < \frac{1}{n}\|\varphi_n\|_{H^1(\mathcal{Y}_\ell)}. \tag{21}$$

Setting $\widetilde{\varphi}_n := \varphi_n/\|\varphi_n\|_{H^1(\mathcal{Y}_\ell)}$, we have

$$\|\nabla\widetilde{\varphi}_n\|_{L^2(\mathcal{Y}_\ell)} < \frac{1}{n}\|\widetilde{\varphi}_n\|_{H^1(\mathcal{Y}_\ell)} \quad \text{with} \quad \|\widetilde{\varphi}_n\|_{H^1(\mathcal{Y}_\ell)} = 1. \tag{22}$$

Since $\widetilde{\varphi}_n$ is bounded in $H^1(\mathcal{Y}_\ell)$, up to a subsequence, one has

$$\widetilde{\varphi}_n \rightharpoonup \widetilde{\varphi} \ \text{ in } \ H^1(\mathcal{Y}_\ell), \quad \widetilde{\varphi}_n \to \widetilde{\varphi} \ \text{ in } \ L^2(\mathcal{Y}_\ell), \tag{23}$$

where "$\rightharpoonup$" denotes weak convergence (See Ref. [1, 7, 9]). Since by (22), one has $\nabla\widetilde{\varphi} = 0$, i.e., $\widetilde{\varphi} = const$. This constant vanishes since $\int_\Theta \widetilde{\varphi}_n\,dz = 0$ and $\int_\Theta \widetilde{\varphi}_n \to \int_\Theta \widetilde{\varphi}$. Then, we have

$$\widetilde{\varphi}_n \to 0 \quad \text{in} \quad H^1(\mathcal{Y}_\ell), \tag{24}$$

which contradicts $\|\widetilde{\varphi}_n\|_{H^1(\mathcal{Y}_\ell)} = 1$ in (22). This completes the proof. □

Theorem 4. *∇u_∞ is periodic in the x-direction such that*

$$\nabla u_\infty(x+1,z) = \nabla u_\infty(x,z) \quad \textit{for} \ \ (x,z) \in \mathcal{Y}_{\ell_0} \ \ \textit{almost everywhere.}$$

Because the similar argument used in the proof of Theorem 3 can be applied, we omit the proof.

Corollary 5. *The limit u_∞ is decomposed into a periodic function u^p in the x-direction and a harmonic function u^h with respect to the x variable:*

$$u_\infty = u^p + u^h, \tag{25}$$

where u^p and u^h are given by

$$u^p(x,z) = u_\infty(x,z) - \left(\int_0^1 \frac{\partial u_\infty}{\partial x}(t,z)\,dt\right)x, \tag{26}$$

$$u^h(x,z) = \left(\int_0^1 \frac{\partial u_\infty}{\partial x}(t,z)\,dt\right)x. \tag{27}$$

Proof. Showing $\partial_{xx} u^h = 0$ is straightforward. Now, we show that $u^p(x+1,z) = u^p(x,z)$. It follows from (26) that

$$u^p(x+1,z) = u_\infty(x+1,z) - \left(\int_0^1 \frac{\partial u_\infty}{\partial x}(t,z)\,dt\right)(x+1). \tag{28}$$

Note that by Theorem 4, $\partial_x u_\infty$ is periodic in the x-direction. It follows from the periodicity of $\partial_x u_\infty$ and (28) that

$$u^p(x+1,z) = u_\infty(x+1,z) - \left(\int_x^{x+1} \frac{\partial u_\infty}{\partial x}(t,z)\,dt\right)(x+1), \tag{29}$$

$$= u_\infty(x,z) - \left(\int_0^1 \frac{\partial u_\infty}{\partial x}(t,z)\,dt\right)x, \tag{30}$$

$$= u^p(x,z). \tag{31}$$

This completes the proof. □

At last, in the aid of Corollary 5, we can define the directional effective conductivity as (the harmonic average of) the inverse of the slope of u^h:

$$\sigma^{ef} := \left(\frac{1}{|\Theta|}\int_\Theta \frac{\partial u^h}{\partial x}(0,z)\,dz\right)^{-1}. \tag{32}$$

Here, we took the harmonic average of the inverse of the slope of u^h over Θ.

Remark 6. *If σ is independent in z variable, i.e., $\partial_z \sigma = 0$, then σ^{ef} is the harmonic average of σ over the cell $\{x\ : 0 < x < 1\} \times \Theta$:*

$$\sigma^{ef} = \left(\frac{1}{|\Theta|}\int_\Theta \int_0^1 \frac{1}{\sigma(x,z)}\,dx\,dz\right)^{-1}. \tag{33}$$

4. Experiment

To test the performance of our reconstruction algorithm (10), we conducted numerical simulations on a rectangular domain. The domain is discretized into 6×11 rectangles as shown Figure 12. We consider various cases of pressure distributions p_{ij} shown in (a) and (c) of Figure 12-13. Given p_{ij}, the measured voltage differences $\delta V_p^{(1)}$ and $\delta V_p^{(2)}$ are computed by (8) and (9), where we assumed that the amount of voltage change for pressure applied at one pixel

is unit ($\beta = 1$). The pressure distributions are reconstructed by using the formula (10) to obtain $\widetilde{p}_{ij}$. Figure 12(b) and (d) are the reconstructed images corresponding to (a) and (c), respectively. In Figure 12, we observe that the proposed algorithm identically recovers the pressure distribution. Figure 13 shows that the proposed algorithm produces the same reconstructed images for different pressure distributions. In this case, the proposed algorithm does not uniquely recover pressure distribution.

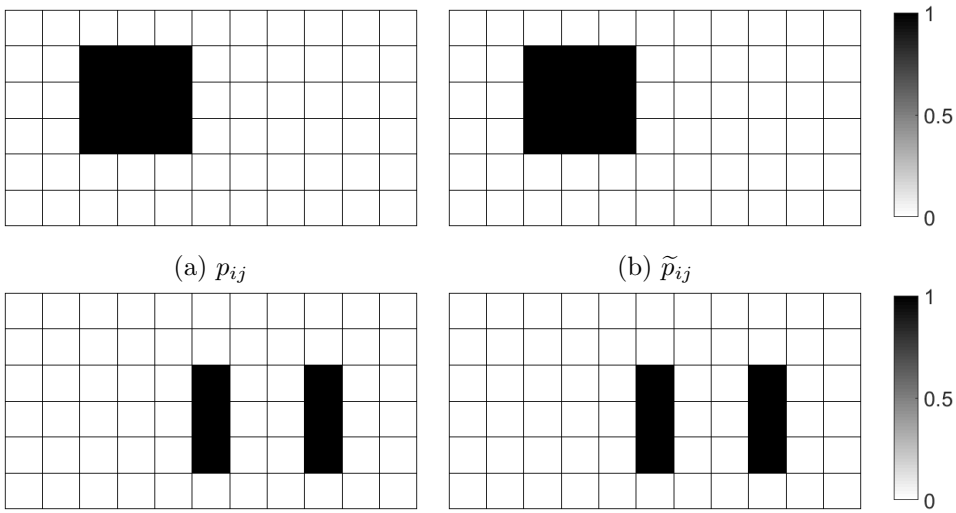

(a) p_{ij} (b) $\widetilde{p}_{ij}$

(c) p_{ij} (d) $\widetilde{p}_{ij}$

Figure 12: Pressure distribution reconstruction. (a) and (c) true pressure distribution p_{ij}; (b) and (d) the reconstructed pressure distributions $\widetilde{p}_{ij}$ by the proposed formula (10).

We test the feasibility of the proposed sensor by validating the effective conductivity change with pressure. For the test, we made a simple composite fabric by weaving a conductive fabric into a non-conductive sponge with high pore density as shown on Figure 14. Here, the conductive fabric is manufactured by Eeonyx (NW170-SLPA-2000), and its surface resistivity is 2000 ohm per square. For the non-conductive sponge, we used a melanin sponge that is commonly used for cleaning purpose. We use the four-electrode method to measure the effective conductivity of the fabric sheet; one pair of electrodes is

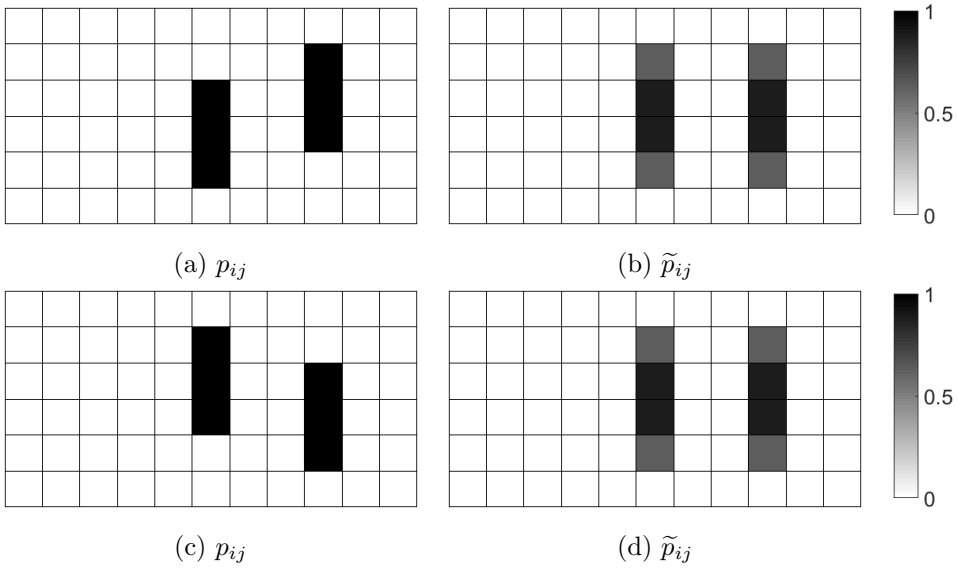

Figure 13: Pressure distribution reconstruction. (a) and (c) true pressure distribution p_{ij}; (b) and (d) the reconstructed pressure distributions $\widetilde{p}_{ij}$ by the proposed formula (10).

used to inject the current and the other pair of electrodes is used to measure the resulting voltage drop. We use Sciospec 8-channel EIT system to inject a sinusoidal current of $1mA$ at $1kHz$ and measure the resulting voltage drop every 0.04 seconds.

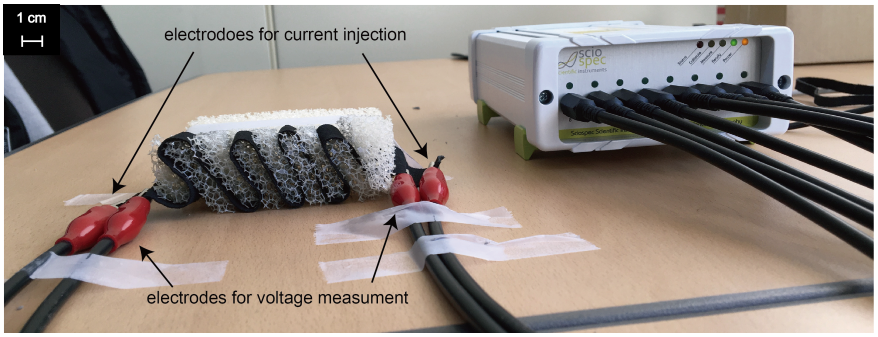

Figure 14: The pressure sensor and Sciospec EIT system

During the current-voltage measurement, we apply a vertical pressure on the upper surface of the composite sponge to observe the change in voltage

drop. Figure 15 illustrates voltage versus time plot. It shows that the change in voltage with the pressure is significant. According to Ohm's law, this change in voltage with pressure implies the increase of the homogenized conductivity.

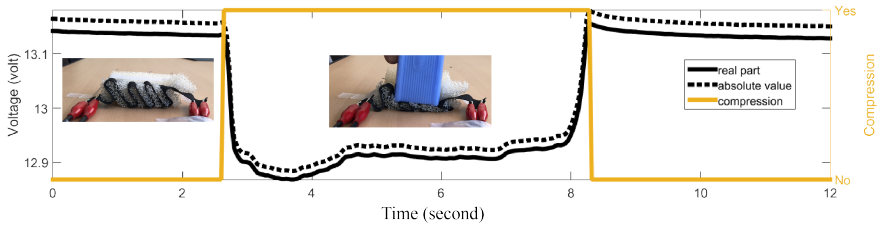

Figure 15: The measured voltages over time.

5. Conclusions

We have proposed a potentially manufacturable flexible pressure sensor and its mathematical model, where the sensor is intended to visualize the pressure distribution applied over the surface of it. This sensor is made of a double layer of thin composite fabric, which is a sponge-like, non-conductive fabric woven with electrically conductive yarns in a wavy pattern along a transverse direction. Here, the weaving directions of the upper layer and the lower layer are selected independently. When current flows along the conductive yarn inside each composite fabric, the directions of the current flowing through the upper layer and the lower layer are independent. A number of electrodes are attached on the edge of the sensor to inject electrical currents and to measure the induced voltages for recovery of the pressure distribution. When pressure is applied to the surface of the sensor, the composite fabrics are locally compressed. The conductive yarns in the compressed region come into contact, resulting in a decrease in impedance. In the proposed mathematical model, the sensor is described in a two-dimensional domain. In order to describe the electrical properties of the sensor in this two-dimensional domain, we performed an asymptotic analysis and defined the effective conductivity. This effective conductivity can be seen as the harmonic average of the conductivities of the conductive yarns and the

sponge-like fabrics. The decrease in impedance due to compression can be interpreted as an increase in the effective conductivity. In order to recover the pressure distribution, we have proposed a back-projection type algorithm and verified the performance by numerical experiment. We then made a simplified sensor and conducted an experiment to show the existence of a pressure-sensitive composite fabric.

The double-layered sensor, which uses two independent currents, may not be sufficient to recover the pressure correctly as show in Figure 13. For better accuracy and to obtain more voltage data (induced by the various currents), one may employ more layers to induce more independent currents in various directions.

As the experiment showed in section 4, while the simplified sensor is pressure-sensitive, it is only able to verify whether pressure is applied to the sensor. However, it does not identify the region(s) where the pressure is being applied. In order to make more useful sensors, more impedances should be measured. This requires EIT systems that have many channels. Note that in order to inject n number of currents and measure n different impedances at the same time, we need an EIT system that has at least $4n$ channels: $2n$ channels for injecting n number of different currents and the other $2n$ for measuring n number of voltage differences.

Acknowledgment

This work was supported by the National Research Foundation of Korea (NRF) grant funded by NRF grant 2015R1A5A1009350. The research of the first author leading to these results has received funding from Lithuanian-Swiss cooperation programme to reduce economic and social disparities within the enlarged European Union under project agreement No CH-3-SMM-01/0.

References

[1] R. A. Adams, *Sobolev Spaces* (Academic Press, 2003).

[2] O. Atalay, W. R. Kennon and M. D. Husain, Textile-Based Weft Knitted Strain Sensors: Effect of Fabric Parameters on Sensor Properties, *Sensors.* **13** (2013) 11114–11127.

[3] G. H. Büscher, R. Kõiva, C. Schürmann, R. Haschke and H. J. Ritter, Flexible and stretchable fabric-based tactile sensor, *Robotics and Autonomous Systems* **63** (2015) 244–252.

[4] M. Cheney, D. Isaacson and J. C. Newell, Electrical impedance tomography, *SIAM Review* **41** (1999) 85–101.

[5] A. Chiolerio, I. Roppolo and M. Sangermano, Radical diffusion engineering: tailored nanocomposite materials for piezoresistive inkjet printed strain measurement, *RSC Adv.* **3** (2013) 3446–3452.

[6] A. Chiolerio, M. Lombardi, A. Guerriero, G. Canavese, S. Stassi, R. Gazia, V. Cauda, D. Manfredi, A. Chiodoni, A. Verna, M. Cocuzza, L. Montanaro and C. F. Pirri, Effect of the fabrication method on the functional properties of $BaTiO_3$: PVDF nanocomposites, *Journal of Materials Science* **48** (2013) 6943–6951.

[7] M. Chipot, *Elliptic Equations: An Introductory Course* (Birkhäuser, 2009).

[8] A. Cömert, M. Honkala and J. Hyttinen, Effect of pressure and padding on motion artifact of textile electrodes, *BioMed. Eng. OnLine* **12** (2013).

[9] G. B. Folland, *Real Analysis: Modern Techniques and Their Applications* (Wiley, 2007).

[10] X. Han, Y. Liu and Y. Yin, Colorimetric stress memory sensor based on disassembly of gold nanoparticle chains, *Nano Letters* **14** (2014) 2466–2470.

[11] D. S. Holder, Electrical impedance tomography: Methods, History and Applications, *IOP Publishing*, Bristol and Philadelphia (2005).

[12] J. Lee, H. Kwon, J. Seo, S. Shin, J. H. Koo, C. Pang, S. Son, J. H. Kim, Y. H. Jang, D. E. Kim and T. Lee, Conductive Fiber-Based Ultrasensitive

Textile Pressure Sensor for Wearable Electronics, *Advanced materials* **27** (2015) 2433–2439.

[13] F. Lorussi, W. Rocchia, E. P. Scilingo, A. Tognetti and D. D. Rossi, Wearable, redundant fabric-based sensor arrays for reconstruction of body segment posture, *IEEE Sensors Journal* **4** (2004) 807–818.

[14] J. F. Saenz-Cogollo, M. Pau, B. Fraboni and A. Bonfiglio, Pressure Mapping Mat for Tele-Home Care Applications, *Sensors.* **16** (2016) 365.

[15] J. K. Seo and E. J. Woo, *Nonlinear Inverse Problems in Imaging* (Wiley, 2013).

[16] M. Stoppa and A. Chiolerio, Wearable Electronics and Smart Textiles: A Critical Review, *Sensors.* **14** (2014) 11957–11992.

[17] S. S. Swallow and A. Peta-Thomson, Conductive pressure sensitive textile, *U.S. Patent* 7365031 B2 (2008).

[18] D. S. Tawil, D. Rye and M. Velonaki, Improved image reconstruction for an EIT-based sensitive skin with multiple internal electrodes, *IEEE Transactions on Robotics* **27** (2011) 425–435.

[19] T. Tommasi, A. Chiolerio, M. Crepaldi and D. Demarchi, A microbial fuel cell powering an all-digital piezoresistive wireless sensor system, *Microsystem Technologies* **20** (2014) 1023-1033.

[20] A. Yao and M. Soleimani, A pressure mapping imaging device based on electrical impedance tomography of conductive fabrics, *Sensor Rev.* **32** (2012) 310–317.

[21] A. Yao, C. L. Yang, J. K. Seo and M. Soleimani, EIT-based fabric pressure sensing, *Comput. Math. Methods Med.* **2013** (2013) 1–9.

[22] G. L. Zeng, *Medical Image Reconstruction* (Springer, 2010).